



HAL
open science

Effects of Chlorine Mixing on Optoelectronics, Ion-Migration and Gamma-ray Detection In Bromide Perovskites

Nikita Rybin, Dibyajyoti Ghosh, Jeremy Tisdale, Shreetu Shrestha, Michael Yoho, Duc Duy Vo, Jacky Even, Claudine Katan, Wanyi Nie, Amanda J Neukirch, et al.

► **To cite this version:**

Nikita Rybin, Dibyajyoti Ghosh, Jeremy Tisdale, Shreetu Shrestha, Michael Yoho, et al.. Effects of Chlorine Mixing on Optoelectronics, Ion-Migration and Gamma-ray Detection In Bromide Perovskites. *Chemistry of Materials*, 2020, 32 (5), pp.1854-1863. 10.1021/acs.chemmater.9b04244 . hal-02478539

HAL Id: hal-02478539

<https://hal.science/hal-02478539>

Submitted on 17 Mar 2020

HAL is a multi-disciplinary open access archive for the deposit and dissemination of scientific research documents, whether they are published or not. The documents may come from teaching and research institutions in France or abroad, or from public or private research centers.

L'archive ouverte pluridisciplinaire **HAL**, est destinée au dépôt et à la diffusion de documents scientifiques de niveau recherche, publiés ou non, émanant des établissements d'enseignement et de recherche français ou étrangers, des laboratoires publics ou privés.

Effects of Chlorine Mixing on Optoelectronics, Ion-Migration and Gamma-ray Detection In Bromide Perovskites

Nikita Rybin,^{†,‡} Dibyajyoti Ghosh,^{*,‡,¶} Jeremy Tisdale,[§] Shreetu Shresta,[§] Michael
Yoho,^{||} Duc Vo,^{||} Jacky Even,[⊥] Claudine Katan,[#] Wanyi Nie,[§] Amanda Joy
Neukirch,[‡] and Sergei Tretiak^{*,‡,¶,@}

[†]*Skolkovo Institute of Science and Technology, Moscow 121205, Russia*

[‡]*Theoretical Division, Los Alamos National Laboratory, Los Alamos, NM, 87545, USA*

[¶]*Center for Nonlinear Studies, Los Alamos National Laboratory, Los Alamos, NM, 87545,
USA*

[§]*Materials Physics and Applications Division, Los Alamos National Laboratory, Los
Alamos, NM, 87545, USA.*

^{||}*Nuclear Engineering and Nonproliferation Division, Los Alamos National Laboratory, Los
Alamos, NM, 87545, USA.*

[⊥]*Univ Rennes, INSA Rennes, CNRS, Institut FOTON - UMR 6082, F-35000 Rennes,
France*

[#]*Univ Rennes, ENSCR, INSA Rennes, CNRS, ISCR - UMR 6226, F-35000 Rennes,
France*

[@]*Center for Integrated Nanotechnologies, Los Alamos National Laboratory, Los Alamos,
NM, 87545, USA*

E-mail: dibyajyoti@lanl.gov; serg@lanl.gov

Abstract

Controlled anion-mixing in halide perovskites has been shown to be an effective route to precisely tuning optoelectronic properties, in order to achieve efficient photovoltaic, light emission and radiation detection devices. However, an atomistic understanding behind the precise mechanism impacting the performances of mixed halide perovskite devices, particularly as a radiation detector, is still missing. Combining high-level computational methods and multiple experiments, here we systematically investigate the effect of chlorine (Cl) incorporation on the optical and electronic properties, structural stability, ion-migration as well as the γ -ray radiation detection ability of $\text{MAPbBr}_{3-x}\text{Cl}_x$. We observe that precise halide mixing suppresses bromide ion migration and consequently reduces the dark current by close to a factor of two, which significantly increases the resistance of the mixed-anion devices. Furthermore, reduced carrier effective masses and mostly unchanged exciton binding energies indicate enhanced charge carrier transport for these perovskite alloys. At the atomistic level, modifications to ion migration and charge carrier transport properties improve electronic properties and predominantly contribute to the better response and resolution in high-energy γ -ray detection with $\text{MAPbBr}_{3-x}\text{Cl}_x$, as compared to MAPbBr_3 . This study provides a systematic approach to enhance the high-energy radiation detection ability of $\text{MAPbBr}_{3-x}\text{Cl}_x$ -based devices by understanding the atomistic properties underpinning performance.

Introduction

Halide hybrid and inorganic perovskites have emerged as some of the most promising candidates for next-generation photovoltaic materials in the last decade.¹⁻⁷ In addition to solar cells, these materials demonstrate potential in various applications, ranging from light emitting diodes and photodetectors, to high-energy radiation sensors.⁸⁻¹⁰ The realization of several beneficial properties like long and balanced diffusion lengths for electrons and holes, high absorption coefficients spanning the entire visible range, robust defect tolerance, and

1
2
3 highly tunable optical band gaps make halide perovskites very attractive materials for a
4 wide range of applications.^{11–13} Particularly, the presence of heavy elements in these dense
5 materials, along with outstanding charge transport properties, indicate their potential use as
6 detectors for high-energy radiations.^{8,14–17} Preliminary studies have reported γ -ray detection
7 with a reasonable resolution using bromide-based hybrid perovskites.¹⁸
8
9
10
11
12

13 Compositional engineering of halides has widely been adopted to improve the stability
14 and enhance the performance of halide perovskite devices.^{19–27} Several groups have explored
15 halide mixing in detail for multivarious purposes such as color management, better crys-
16 tallization and tuning the band gaps for tandem solar cells.^{11,28–31} Due to the numerous
17 beneficial effects, most of the highly efficient perovskite solar cells are of mixed halide com-
18 positions. In this regard, chlorine (Cl) incorporation was reported to dramatically improve
19 diffusion lengths of carriers in MAPbI₃.^{11,28–30} However, the presence of Cl in bulk MAPbI₃
20 and its exact impact on the optoelectronic properties has been highly debated in recent
21 years.^{31–34} Most of the reports have indicated that Cl can form a solid solution with Br and
22 stay in the bulk of MAPbBr₃.^{35–37} The relatively small difference in ionic radii and elec-
23 tronegativity between Br and Cl allows these anions to form solid solutions of mixed-anion
24 halide perovskites. Due to the large band gap (> 2 eV), bromide based perovskites are not
25 suitable for single-junction solar cells. However, they have been extensively used for LEDs
26 and photodetector devices.^{8,9,38,39} Cl incorporation in MAPbBr₃ precisely tunes the emission
27 color for LEDs and response spectrum for photodetectors. Furthermore, MAPbBr_{3-x}Cl_x thin
28 films exhibit significantly prolonged recombination lifetime with finely tuned Cl concentra-
29 tions. For high-energy radiation detection, MAPbBr₃ is one of the first hybrid perovskite
30 materials to show promising results with significant response to charged particles.^{40,41} After-
31 wards, hybrid and non-hybrid lead halide perovskites showed promising results for low-cost
32 γ -ray detectors, including MAPbI₃,⁴² and CsPbBr₃.¹⁵ It was shown later that MAPbBr₃
33 responds not only to charged particles, but also to neutrons and γ -rays. However, the re-
34 sponse to γ -ray was found to be weak for this material.⁴³ Nevertheless, recent experiments
35
36
37
38
39
40
41
42
43
44
45
46
47
48
49
50
51
52
53
54
55
56
57
58
59
60

1
2
3 have demonstrated the positive influence of Cl incorporation in MAPbBr₃, such as increased
4 resistivity and reduced device noise of these materials. A small Cl concentration ($\approx 2\%$ mo-
5 lar ratio) has been found to dramatically enhance the resolution for γ -ray detection under
6 a small electric field.¹⁸ Despite all of these fascinating reports, a systematic and in-depth
7 atomistic understanding on the effects of anion mixing for γ -ray detection of MAPbBr_{3-x}Cl_x
8 is largely absent.
9
10

11
12
13
14
15 In the present work, we combine experimental and computational efforts to thoroughly
16 investigate the optoelectronic properties of MAPbBr_{3-x}Cl_x, particularly focusing on the small
17 Cl concentration range ($x \leq 0.45$). We demonstrate that within this concentration regime,
18 Cl is incorporated into the bulk of the material. Our atomistic level investigations find that
19 anion-mixing partially suppresses the Br migration and enhances the charge carrier transport
20 in these materials. These modifications significantly benefit the γ -ray detection response at
21 room temperature. This study offers a guideline for improving radiation detection properties
22 of hybrid bromide perovskites with an in-depth atomistic understanding of compositional
23 tuning.
24
25
26
27
28
29
30
31
32
33

34 35 Results and Discussion

36
37
38 First, we evaluate numerically the thermodynamic stability of mixed anion MAPbBr_{3-x}Cl_x
39 lattices with respect to the corresponding monoanionic perovskites. As shown in Figure 1a,
40 the calculated Helmholtz free energy (see Methods and section S1 in SI for details) of mixing
41 for all the studied Cl concentrations is negative, indicating a stabilized solid solution of Br and
42 Cl in these lattices. With increasing temperature, the solid solutions become more stable due
43 to a significant entropic contribution to the free energy of mixing. Thus, our computational
44 study indicates incorporation of Cl into the bulk of MAPbBr₃, forming mixed Br/Cl lattices.
45 These results are in agreement with recent experimental and computational studies, where
46 solid solution formation has been reported for Br/Cl mixing at room temperature.⁴⁴⁻⁴⁹ Two
47
48
49
50
51
52
53
54
55
56
57
58
59
60

1
2
3 competing factors, strengths of ionic Pb-X bonds (X=Cl, Br) and strain energy due to the
4 size mismatch between halides, dominantly affect the internal energies of $\text{MAPbBr}_{3-x}\text{Cl}_x$
5 crystals.^{49,50} Compared to Br, Cl atoms form stronger ionic bonds with Pb^{2+} due to their
6 higher electronegativity. As reported for similar perovskites, these stronger ionic bonds yield
7 sufficient Coulomb energy to overcome the strain energy that arises from the size mismatch
8 between the halide atoms.^{49,50} Thus, at a lower concentration limit (up to 25 mol%), the solid
9 solution of anions shows increased stability compared to the phase separated constituents
10 of MAPbBr_3 and MAPbCl_3 . The entropy of mixing, which arises due to anion mixing,
11 stabilizes the mixed anion lattices further, exhibiting prominent thermodynamic stability of
12 $\text{MAPbBr}_{3-x}\text{Cl}_x$ at room temperature. Similar entropy of mixing induced stability has also
13 been reported for mixed A-cation perovskites.^{21,51}

14
15 To provide evidence of controlled anion mixing in the experimental single crystals, we
16 further explore the structural and optical changes in $\text{MAPbBr}_{3-x}\text{Cl}_x$ (Figure 1b-d). As shown
17 in Figure 1b, the experimentally measured unit cell volumes (measured via powder X-ray
18 diffraction on finely ground single crystals) reduce with increased Cl concentration, unam-
19 biguously showing successful anion mixing in these samples. The results shown in Figure
20 S1 and Table S1 exhibit a quasi-linear trend in the experimentally determined cubic lattice
21 parameter values with increased Cl concentration, decreasing from $a = 5.92 \text{ \AA}$ to $a = 5.85$
22 \AA , for MAPbBr_3 and $\text{MAPbBr}_{2.4}\text{Cl}_{0.6}$, respectively. The experimental lattice volume was
23 then calculated based on the $\text{Pm}\bar{3}\text{m}$ cubic structure, as explained in the Experimental Pro-
24 cedure later. Similar lattice contraction in $\text{MAPbBr}_{3-x}\text{Cl}_x$ with increased Cl concentration
25 has been reported previously as well.^{8,45,52-55} It is worth to mentioning that, quasi-linear
26 trend of lattice contraction for Br/Cl-mixed lattices is in agreement with the $\text{MAPbI}_{3-x}\text{Br}_x$
27 systems as reported earlier by Noh *et al.*⁵²

28
29 Computationally optimized ground state structures of orthorhombic $\text{MAPbBr}_{3-x}\text{Cl}_x$ (see
30 Methods) corroborate the trend of reduced lattice parameters and volume with Cl inclusion as
31 shown in Figure 1b (black solid line). Although the extent of the reduction differs, the overall
32
33
34
35
36
37
38
39
40
41
42
43
44
45
46
47
48
49
50

1
2
3 trend in decreasing unit cell volume is in agreement between calculations and experimental
4 observations. The difference in the extent of volume reduction can originate due to the
5 fact that the experimental data corresponds to thermally expanded quasi-cubic structures,
6 where the MA cation rotations are activated, while in the computational study, supercells
7 are of the low-temperature orthorhombic phase with static A-cations. Detailed discussion is
8 included in section S2 in SI. The smaller ionic radii for Cl with respect to Br, (r_{Cl} (1.67 Å)
9 $< r_{\text{Br}}$ (1.84 Å)) and consequently shorter bond length of Pb-Cl than Pb-Br bonds, (see Fig.
10 S2) is the apparent cause for this change in lattice volume. Thus, unlike the $\text{MAPbI}_{3-x}\text{Cl}_x$
11 systems,^{11,28–30,32–34} our combined computational and experimental studies unambiguously
12 demonstrate that at lower concentrations (up to 20 mol%), Cl prefers to be incorporated into
13 the MAPbBr_3 lattice, via substitution of Br atoms, instead of inhomogeneous accumulation
14 on the surfaces and interfaces.

15
16 We further characterize the optical properties of $\text{MAPbBr}_{3-x}\text{Cl}_x$ ($0 \leq x \leq 0.6$). To
17 experimentally study changes in the band gap as a function of Cl incorporation, we examine
18 the UV-Vis absorption (Figure 1c) and photoluminescence (Figure 1d) properties. Because
19 of the 2 mm thick crystals, UV-Vis spectra were extracted from transmission measurements
20 and converted to Tauc plots to estimate the optical band gaps. Other than the calculated
21 band gaps, we also differences among the chlorine concentrated crystals in the above band
22 gap regime of the absorption. For the 0%, 2%, and 5% Cl-incorporated crystals, the band
23 edge is clear, and the above band gap regime is smooth. However, with the 10%, 15% and
24 20% Cl-incorporated crystals, we notice that the band edge is not as sharp with double
25 features and the above band gap regime is noisy. We contribute this to the quality of the
26 crystals grown, as we found when doping with $>10\%$ Cl, the crystal quality heavily decreases,
27 showing cloudiness and microcracks, leading to the noisy signals in the absorption data.

28
29 There is a prominent linear trend, as the band gap of the single crystals increase as a
30 function of Cl concentration (Figure S3a). The photoluminescence (Figure 1d) also shows
31 the same trend, where we observe a gradual blue shift in the band gap of the single crystals
32
33
34
35
36
37
38
39
40
41
42
43
44
45
46
47
48
49
50

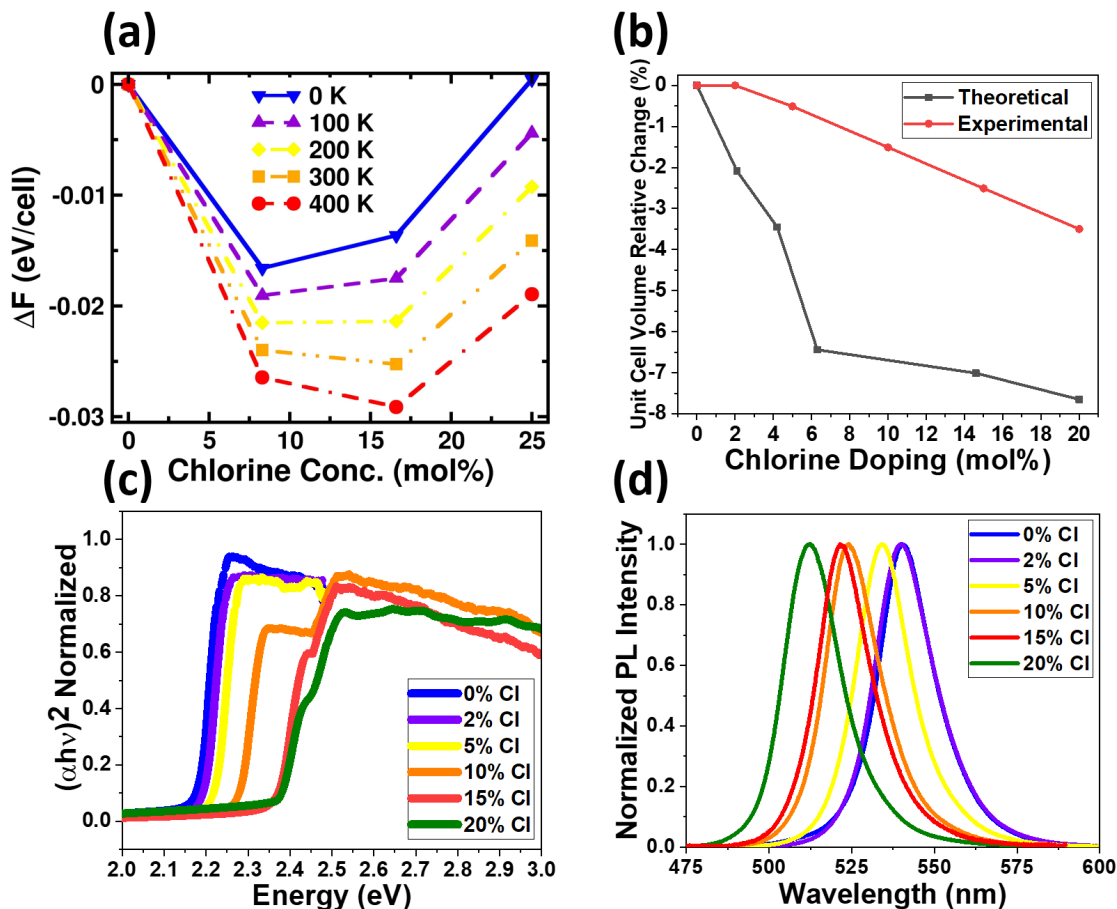


Figure 1: Effect of Cl incorporation in MAPbBr_{3-x}Cl_x. (a) Computational Helmholtz free energy as a function of Cl mol% and temperature, (b) Relative change in unit cell volume as a function of Cl concentration from computational calculations and experimental powder XRD, (c) Experimental UV-Vis absorption spectra and (d) emission spectra.

as the Cl concentration is increased (see Figure S3b). In parallel, we computationally evaluated the band gap variation in these mixed halide perovskites including spin-orbit coupling (SOC) effects for the heavy-element Pb and the hybrid (HSE06) functional (see Methods). As presented in Figure S4, the calculated band gaps blue-shift with the increased Cl concentration, in agreement with the experimental results. Note that, computationally evaluated band gap values are underestimated by ≈ 0.4 eV due to insufficient inclusion of the exact Hartree-Fock exchange term in the HSE06 functional. This systematic underestimation of the band gap using the HSE06 functional is well known and has been previously reported for other halide perovskites.^{13,21,27,56} Moreover, the computed absorption spectra (Figure S5)

1
2
3 and corresponding calculated band gaps (Figure S3) calculated by the semi-local exchange-
4 correlation functional, i.e. GGA-PBE functional, show better agreement with experimental
5 data due to an incidental error cancellation of the SOC and electron-electron interaction
6 terms.⁵⁷
7
8
9

10
11 Next, we investigate the ion migration in these materials and its impact on current-
12 voltage properties of the devices.^{58–60} Ion transport induced phenomena underpin current-
13 voltage hysteresis, switchable photovoltaics and polarization effects, and limit the applica-
14 tion of hybrid perovskites in the field of solar cells and radiation detection.^{61–64} Recently,
15 compositional engineering with A-cations in iodide perovskites has been demonstrated as a
16 promising approach to partially suppress the ion migration.⁶⁵ Here we investigate computa-
17 tionally and experimentally the effect of varying anion composition on the ion migration in
18 MAPbBr_{3-x}Cl_x.
19
20
21
22
23
24
25
26

27 We computationally calculate activation energy barriers for the vacancy-assisted halide
28 ion hopping in these mixed anion perovskites with the dispersion corrected DFT-based climb-
29 ing image nudged elastic band (CI-NEB) approach (see Methods).⁶⁶ Note that we focus only
30 on the halide diffusion, as previous studies report much higher activation barriers for Pb²⁺
31 and MA⁺ ions, due to the significant rearrangements in the local structure.^{65,67,68} Since we
32 have considered the low-symmetry orthorhombic phase of MAPbBr_{3-x}Cl_x, two inequivalent
33 migration paths for Br/Cl have been modeled: (1) Br/Cl migration from equatorial to api-
34 cal site and (2) Br migration from equatorial to equatorial site. In our calculations (see
35 Methods), the initial and final configurations of the migration path were well converged in
36 order to avoid severe underestimation of barrier energies. In MAPbBr₃, we find the acti-
37 vation energies of 0.24 eV and 0.33 eV, for Br migrating from equatorial to equatorial and
38 equatorial to apical site, respectively (see Figure 2a and Figure S6, S7). Similar migration
39 barriers and a relative trend for Br diffusion have been reported by Meloni *et al.* in tetrag-
40 onal MAPbBr₃.⁶⁸ These results suggest that Br diffusion in real crystals occurs both along
41 apical and equatorial directions without having any preferential direction. Consequently,
42
43
44
45
46
47
48
49
50
51
52
53
54
55
56
57
58
59
60

1
2
3 the migration path with the higher activation energy, i.e., equatorial to apical hopping, can
4 be considered as the rate limiting step for overall ion diffusion in this material (Figure S6).
5 Therefore, in $\text{MAPbBr}_{3-x}\text{Cl}_x$ we calculate the activation energies of Br and Cl diffusion only
6 along this high energy migration path. These simulations demonstrate two key results: (1)
7 the activation energy for Cl (0.22-0.23 eV) is smaller than that for Br (0.47-0.59 eV) ions,
8 (Figure S9 and Table S2) and (2) the migration barrier for Br markedly increases with the
9 inclusion of Cl ions from 0.33 eV for MAPbBr_3 to 0.59 eV for $\text{MAPbBr}_{2.75}\text{Cl}_{0.25}$. Overall, the
10 migration barrier for Br steadily raises with the Cl concentration in $\text{MAPbBr}_{3-x}\text{Cl}_x$, as shown
11 in Figure 2a, Figure S6, and Table S2. This indicates limited interdiffusion of halogens as
12 also reported for Cs-based perovskites.⁴⁷ Such change in ion dynamics can be rationalized by
13 the fact that with the addition of smaller Cl ions effective lattice constant reduces. It follows
14 the trend that the larger the anion size, the larger the anion migration barrier, as found
15 by comparing iodide and bromide based perovskites.⁶⁸ Not surprisingly, due to its smaller
16 ionic radii with respect to Br, the Cl diffusion barrier is lower in energy. Even though this
17 indicates more pronounced Cl migration in the lattice, such enhanced ionic motion does not
18 affect overall optoelectronic properties due to relatively low concentrations of Cl and reduced
19 participation of Cl orbitals in near band-gap transitions as analyzed later.

20
21
22
23
24
25
26
27
28
29
30
31
32
33
34
35
36
37 To further investigate an increased Br migration barrier leading to partial suppression,
38 of Br diffusion in $\text{MAPbBr}_{3-x}\text{Cl}_x$, we analyze the local structural distortions adjacent to
39 the migration path of Br. As a characteristic measure of such distortions, we calculate the
40 displacement of the neighboring Pb atom during Br migration. Larger displacements of Pb in
41 $\text{MAPbBr}_{3-x}\text{Cl}_x$ compared to MAPbBr_3 demonstrate stronger geometric distortion in mixed-
42 anion lattices (see Figure S8). As discussed earlier, Cl inclusion spatially contracts the lattice,
43 narrowing the curved migration path for Br in these materials as shown in Figure S7.⁶⁵ This
44 structural change and consequent steric constraints distort the local structure along the
45 migration path of Br, increasing its activation energy. An increase in activation energy for
46 Br with Cl concentration in the lattice further supports the link between volume contraction
47
48
49
50
51
52
53
54
55
56
57
58
59
60

and partially suppressed Br migration. Note that, similar limited halide interdiffusion in $\text{MAPbI}_{3-x}\text{Br}_x$ and $\text{CsPbI}_{3-x}\text{Br}_x$ in presence of Br anions in small concentration has been studied extensively.^{47,69–71} For example, using a combination of experimental techniques, such as impedance spectroscopy and muon spin relaxation, Rodriguez *et al.* demonstrated largely suppressed iodide migration in $\text{MAPbI}_{2.5}\text{Br}_{0.5}$ due to the compact crystal structure of these mixed halide perovskites.⁷⁰

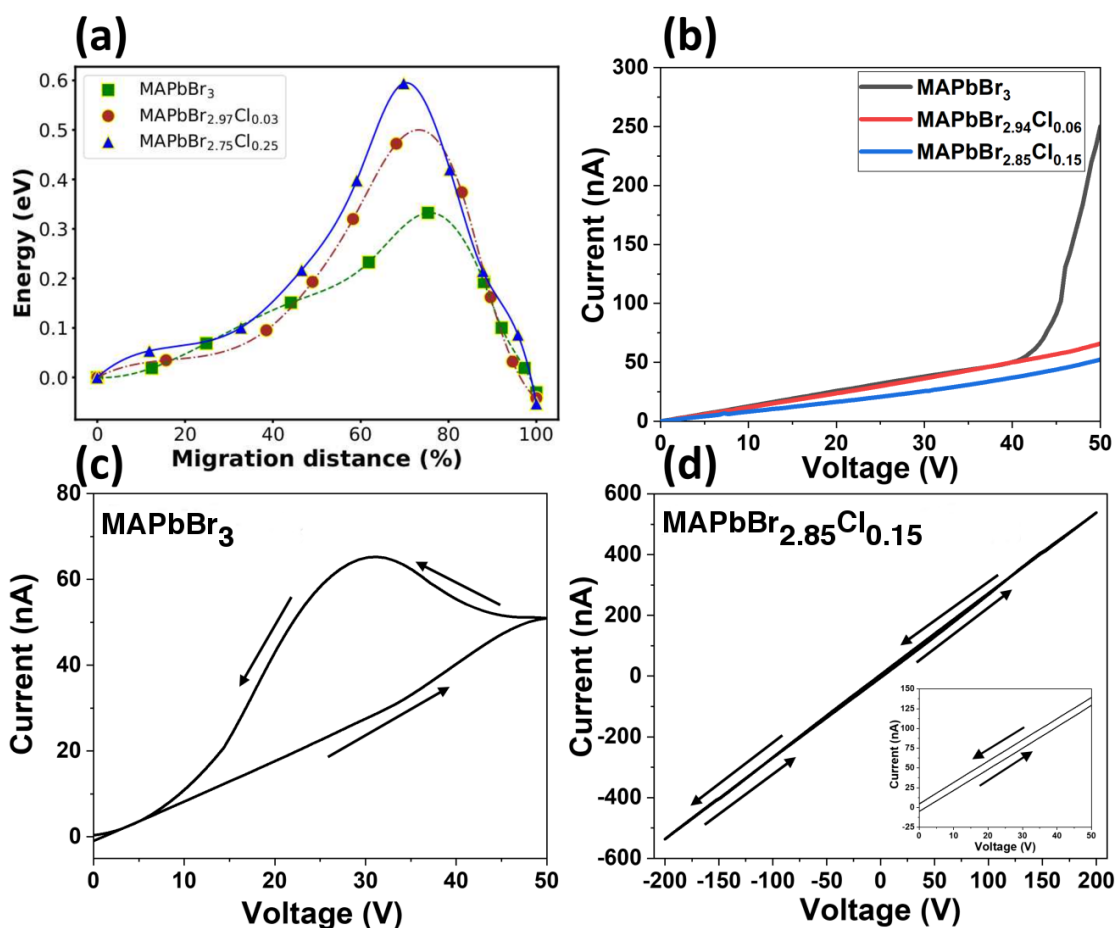


Figure 2: Ion migration in mixed halide perovskites. (a) Minimal energy path for Br ion migration in $\text{MAPbBr}_{3-x}\text{Cl}_x$ with different Cl concentration. (b) Dark current measurements for $\text{MAPbBr}_{3-x}\text{Cl}_x$ for small concentrations. (c) IV hysteresis loop for pure $\text{Cr}/\text{MAPbBr}_3/\text{Cr}$, as compared to the (d) negligible current hysteresis behavior shown for $\text{Cr}/\text{MAPbBr}_{2.85}\text{Cl}_{0.15}/\text{Cr}$ device.

To experimentally validate the partial suppression of Br ion migration in $\text{MAPbBr}_{3-x}\text{Cl}_x$, we measured the dark current at different Cl concentrations to indirectly probe ionic mo-

tion. The dark current for MAPbBr_3 , $\text{MAPbBr}_{2.94}\text{Cl}_{0.06}$, and $\text{MAPbBr}_{2.85}\text{Cl}_{0.15}$ are shown in Figure 2b. The device architecture used for these measurements consisted of a simple metal/semiconductor/metal sandwich architecture, namely Cr/Perovskite/Cr. Cr contacts were used, as it has been shown that Cr contacts create an Ohmic contact between -20 to +20 V with MAPbBr_3 .⁷² This allowed for direct comparisons between device dark current and resistivity based on the results shown in Figure 2b. From 0 to +30V, the devices were fit with linear curves to calculate the low-bias-regime device resistivities. Five devices for each composition were measured to obtain an average resistivity (See Fig. S10). In this bias range, the resistivities of each of the five Cr/perovskite/Cr compositions were calculated (average of three detectors at each composition) as follows : $\rho_{\text{MAPbBr}_3} = 0.295 \pm 0.152 \text{ G}\Omega\cdot\text{cm}$, $\rho_{\text{MAPbBr}_{2.94}\text{Cl}_{0.06}} = 0.745 \pm 0.352 \text{ G}\Omega\cdot\text{cm}$, and $\rho_{\text{MAPbBr}_{2.85}\text{Cl}_{0.15}} = 1.522 \pm 0.156 \text{ G}\Omega\cdot\text{cm}$. It is clear that incorporating small amounts of Cl into the MAPbBr_3 single crystals reduces the dark current, and causes an increase in resistivity, which is required to produce a high signal to noise ratio in applications requiring high bias, such as spectral resolution of γ -rays. We observe that the MAPbBr_3 device has a turn on voltage of around +40 V with large hysteretic behavior, as shown in Figures 2b. Figure 2c was measured with a separate MAPbBr_3 device to show the large variation that exists among different MAPbBr_3 devices. Meanwhile, there is less variation in the Cl-doped crystals, which alludes to more controlled, consistent, high-quality growth for small amounts of Cl-doping. Also, the characteristics for Cl-doped samples stay linear with no signs of severe hysteresis when measured at the same scan speed. This indicates that ion migration is partially suppressed in the Cl-doped MAPbBr_3 single crystals, as current-voltage hysteresis in hybrid perovskite materials has been directly linked to ion migration.⁶¹ To further demonstrate the partial suppression of ion migration, the $\text{MAPbBr}_{2.85}\text{Cl}_{0.15}$ based device was scanned in a loop IV curve, as shown in Figure 2d. This device has minimal hysteresis from -200 V to +200 V, and also shows symmetric negative and positive IV behavior, where we observe a consistent absolute value of current around 540 nA at a bias of ± 200 V. The inset of Figure 2d shows a zoomed-in portion of the IV

1
2
3 curve to compare the MAPbBr₃ to the MAPbBr_{2.85}Cl_{0.15} device. Note that, in Figure 2b we
4 used the forward scans to compare device resistivity among the 0, 2, and 5% Cl-incorporated
5 single crystals. In Figures 2c,d, we aimed to probe the hysteretic behavior of the devices
6 to further understand the properties of the 0, 2, and 5% single crystalline devices. It is
7 clearly seen that there is a minimal hysteresis in the Cl-doped device, as compared to the
8 pure MAPbBr₃ device. This alludes to the fact that the halide mixing in MAPbBr_{3-x}Cl_x
9 single crystals partially suppresses ion migration, leading towards more stable response with
10 negligible hysteresis at large electric fields required for γ -ray spectroscopy.
11
12

13 To further understand the effect of Cl incorporation on the electronic structure, we an-
14 lyzed the partial density of states for MAPbBr_{3-x}Cl_x with HSE06+SOC based DFT simu-
15 lations. As shown in Figures 3a,b and S11,12, the valence band predominantly forms from
16 4p Br and 6s Pb, whereas 6p Pb mainly contributes to the conduction band edge. We
17 find a very small contribution from the Cl orbitals to both the valence band (VB) and the
18 conduction band (CB) edges of these mixed-halide perovskites (Figure S11). Thus, as also
19 shown in Figure 3a and 3b, the delocalized charge density of the VB over the entire Pb-Br
20 framework in MAPbBr₃ becomes partially localized in MAPbBr_{3-x}Cl_x due to the negligible
21 participation of Cl atoms. The localization of the VB charge density upon Cl incorporation
22 can be clearly seen from the plotted band decomposed charge density in Figure 3b. On the
23 contrary, as the CB wave function is dominantly localized over the Pb atoms (Figure S12),
24 it remains mostly unchanged with anion mixing in these materials.
25
26
27
28
29
30
31
32
33
34
35
36
37
38
39
40
41
42

43 Predicted significant influence of Cl mixing on the charge density of the frontier bands
44 further directs us to investigate the charge carrier transport in MAPbBr_{3-x}Cl_x by calculating
45 the effective masses (m^*). Under a constant relaxation-time (τ) approximation, carrier
46 mobilities inversely vary with these effective masses according to the relation, $\mu = e\tau/m^*$,
47 where e is elementary charge. For MAPbBr₃, we evaluate small electron and hole effective
48 masses to be 0.17 and 0.20, (in units of electron mass) respectively, which agrees well with
49 previous experimental and computational reports.^{73,74} Moreover, as shown in Figure 3c, the
50
51
52
53
54
55
56
57
58
59
60

carrier effective masses reduce moderately with increased Cl concentration in $\text{MAPbBr}_{3-x}\text{Cl}_x$, indicating enhanced carrier mobilities in these crystals. Previous experiments have also reported enhanced carrier transport behavior with Br/Cl mixing in halide perovskites.¹⁸ The almost equal effective masses for electrons and holes in these materials also indicates a more balanced charge carrier transport character which is highly desired for efficient γ -ray detector semiconductors.

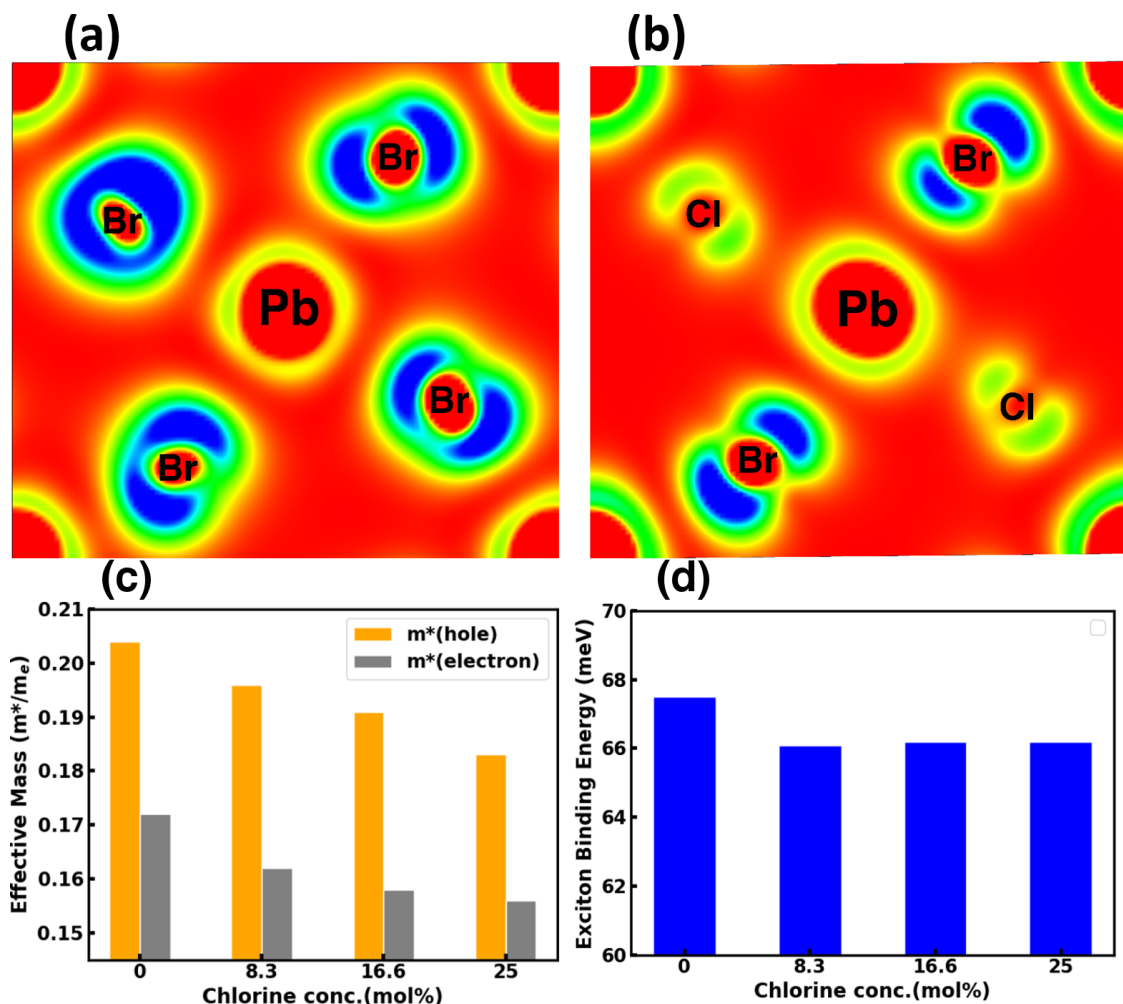


Figure 3: Effect of anion mixing in the electronic properties of $\text{MAPbBr}_{3-x}\text{Cl}_x$ with HSE06+SOC based DFT simulations. Band decomposed charge density for VBM in (a) MAPbBr_3 and (b) $\text{MAPbBr}_{2.25}\text{Cl}_{0.75}$. Color scale for: red is defined as 0 and blue as $0.00025 \text{ e}^- \text{ \AA}^{-3}$. The change in (c) effective masses and (d) exciton binding energies with Cl incorporation.

Recent studies have also identified that the presence of excitons significantly influences

1
2
3 the photophysical properties of bromide and chloride based perovskites.^{73,75,76} Higher exciton
4 binding energies significantly hinders the free charge-carrier generation, ultimately reducing
5 the carrier transport of a photovoltaic material.⁷⁷ Furthermore, experimental reports indi-
6 cate increased exciton binding energies for bromide and chloride based hybrid perovskites
7 compared to that for the iodide one.^{73,78,79} So, the effect of Cl inclusion on the excitonic
8 behavior is important to understand the optoelectronics of $\text{MAPbBr}_{3-x}\text{Cl}_x$. We computa-
9 tionally evaluate the exciton binding energies (details of calculation are included in Methods
10 section) for these mixed halide perovskites as shown in Figure 3d. As discussed in previous
11 studies, we considered the excitons as the Mott-Wannier type for which the effective Bohr
12 diameter is much larger than the host lattice constant.^{12,80} Within this model, we calculate
13 the exciton binding energy as 67 meV for MAPbBr_3 , agreeing very well with previous optical
14 absorption and magneto-absorption based experimental reports.^{81,82} Further exploring mixed
15 halide perovskites, the binding energies are found to be very similar for all $\text{MAPbBr}_{3-x}\text{Cl}_x$,
16 depicting negligible effects of Cl mixing towards the excitonic nature of these lattices. Simul-
17 taneous lowering of reduced effective masses and a high-frequency dielectric constant (see
18 Figure S12) makes the exciton binding energy mostly insensitive to the anion mixing in these
19 perovskites. Thus, our study indicates that Cl inclusion does not affect the excitonic nature
20 of the charge carrier transport in these halide perovskites.

21
22
23
24
25
26
27
28
29
30
31
32
33
34
35
36
37
38
39 Finally, we demonstrate the importance of Cl incorporation in the MAPbBr_3 perovskite
40 single crystals in regards to high-energy γ -ray radiation detection (Figures 4a-c). We fab-
41 ricated devices with a structure of $\text{Cr}/\text{MAPbBr}_{3-x}\text{Cl}_x/\text{Cr}$ to test for γ -ray responses. Ten
42 different devices were tested using pure MAPbBr_3 as the radiation absorbing semiconductor
43 single crystal. When exposed to ^{241}Am source, all of the devices showed no appreciable pulses
44 above the baseline on the oscilloscope. This may be due to the lower resistivity of MAPbBr_3 ,
45 where the noise to signal ratio is too low to resolve γ -rays. However, with $\text{MAPbBr}_{2.85}\text{Cl}_{0.15}$
46 based devices, we observed many clear pulses. Figures 4b and 4c show two of the analyzed
47 pulses obtained from $\text{MAPbBr}_{2.85}\text{Cl}_{0.15}$. Note that we use $\text{MAPbBr}_{2.85}\text{Cl}_{0.15}$ for γ -ray detec-
48
49
50
51
52
53
54
55
56
57
58
59
60

tion as this composition results in the lowest dark current. Here, we observe that increasing the electric field through the device results in a larger pulse/signal amplitude and faster rise time (represented as 10% to 90% of the rise in the pulse), as expected. At room temperature, after counting for 5 minutes, the spectrum for ^{241}Am source was collected as shown in Figure 4a, with a spectral resolution of 35%. While the resolution of the photopeak is low, it is in agreement with previous reports exploring other hybrid perovskite compositions.^{83,84}

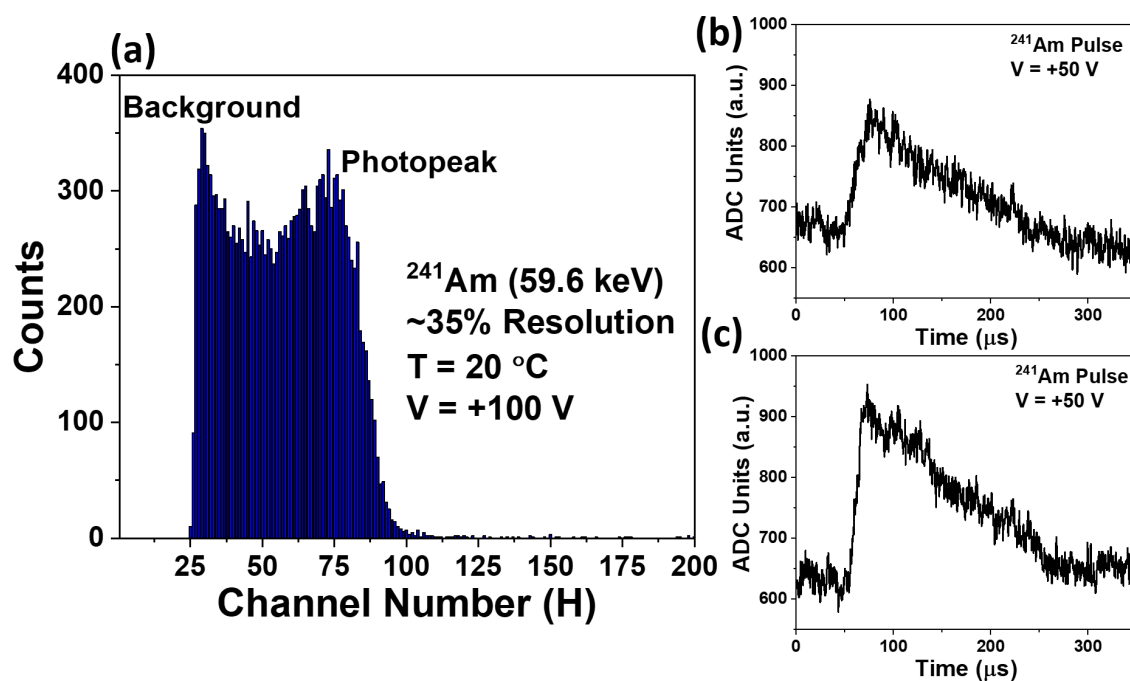


Figure 4: (a) Energy resolved spectrum of 59.6 keV-rays from a ^{241}Am source using a Cr/MAPbBr_{2.85}Cl_{0.15}/Cr device structure. (b,c) ADC (analog to digital converter) traces of pulses obtained from single photon counting with the device from ^{241}Am . Both pulses recorded at room temperature, with a bias of +50 V and +100V, respectively.

For a halide perovskite based γ -ray detector, the presence of high dark current, particularly under high electric field, strongly introduces electronic noise which adversely affects the resolution of the semiconductor detector. We find that ion-migration mediated dark current can be strongly suppressed by controlled anion mixing in MAPbBr_{3-x}Cl_x, consequently reducing electronic noise in the device and resulting in a prominent γ -ray spectrum for ^{241}Am . Enhanced and more balanced charge carrier transport is another influential factor for these detectors, as it ensures efficient charge collection in the devices. An overall increase of the car-

rier mobilities in $\text{MAPbBr}_{3-x}\text{Cl}_x$, indicated by decreasing effective masses as a function of Cl concentration, depicts improved carrier transport in these materials. Improvement in the signal to noise ratio, increase in device resistivity, and enhanced and balanced charge transport due to anion mixing, are a few of the major influences on strong γ -ray radiation response in these $\text{MAPbBr}_{3-x}\text{Cl}_x$ perovskite single crystals. With three $\text{Cr}/\text{MAPbBr}_{2.85}\text{Cl}_{0.15}/\text{Cr}$ working devices, we tested the response to ^{241}Am photons on a regular basis once a week to get a general idea of the device stability. In these experiments, no degradation was readily visible as the strong response and signal to noise ratio was observable every measurement for 8 to 12 weeks. Each time the devices were stored in the dark (inside a laboratory drawer). After this time period, devices stopped responding to γ -ray photons, possibly due to material degradation. We plan to conduct follow up studies to more deeply understand the device stability and what types of degradation cause instabilities over time.

In conclusion, anion-mixing in single crystal growth of the $\text{MAPbBr}_{3-x}\text{Cl}_x$ hybrid perovskite is an efficient and simple synthetic route of tuning optoelectronic properties of these materials. In this work, our combined experimental and computational techniques bring detailed information on how anion mixing affects physical processes related to high energy radiation detection across multiple length-scales. Incorporation of Cl is homogeneous in the bulk of $\text{MAPbBr}_{3-x}\text{Cl}_x$. In particular, we demonstrate that this processes efficiently suppress Br ion migration. Reduced effective carrier masses and almost unaffected exciton binding energies further underpin enhanced optoelectronic properties for these Cl-mixed perovskites. These improved properties result in a prominent increase in γ -ray detection ability for $\text{MAPbBr}_{3-x}\text{Cl}_x$ compared to pristine MAPbBr_3 . Therefore, this study provides a deep atomistic understanding of the effects of anion mixing in hybrid perovskites, and suggests materials design strategies to enhance high-energy radiation detection using these materials.

Methods

Computational Details

Geometry relaxation and electronic structure calculations were performed within density functional theory (DFT)-based simulations as implemented in the Vienna Ab Initio Simulation Package (VASP).^{85,86} The projected augmented wave (PAW) method, Van der Waals correction as described by Grimme and generalized gradient approximation (GGA) with the Perdew-Burke-Ernzerhof functional (PBE) for the exchange and correlation interactions have been considered.⁸⁷⁻⁸⁹ To compute the impact of Cl inclusion with experimental concentrations of as low as 2% to the crystal structure, a large $2\times 2\times 1$ supercell (16 formula unit) of the parent MAPbBr_3 was considered. Unit cell (4 formula units) of orthorhombic MAPbBr_3 which is stable at low temperature has been considered as the parent system for all the electronic structure simulations. Note that, as orthorhombic MAPbBr_3 shows dynamical stability, we considered this phase for all our simulations.⁹⁰ Structure optimization is considered to be converged when the maximum residual force on each atom becomes smaller than $0.01 \text{ eV}/\text{\AA}$. Self-consistent calculations for electronic structure calculations are performed including spin-orbit coupling corrections and considering screened hybrid functionals of Heyd-Scuseria-Ernzerhof (HSE06) unless otherwise stated. The Brillouin-zones are sampled with $4\times 4\times 4$ and $2\times 2\times 2$ Monkhorst-Pack k-point mesh for geometry optimization and HSE06-SOC based self-consistent calculations, respectively. Details of Helmholtz Free Energy calculations are described in SI (Section S1). The carrier effective masses were calculated using least-squares fit for parabolic band dispersion.⁹¹ The high-frequency dielectric constants were evaluated within independent particle approximation. Activation energies for ion transport processes were evaluated from the total energy difference between the diffusing anions (i.e. Br or Cl) in their ground-state configuration and at the saddle point of the hopping process. For these simulations, we considered very large $2\times 2\times 2$ supercell (32 formula units) to ensure that ion migration path does not get influenced by the spurious

1
2
3 periodic defect images. Here ion diffusion has been modeled by single-hopping of ions to the
4 nearest ion vacancy site inside the supercell. Climbing-image nudged elastic band (CI-NEB)
5 methodology as implemented by Henkelman has been used to determine the minimum en-
6 ergy path (MEP) for the ion transport.⁶⁶ Ten images were considered along the MEP to
7 model the migration path accurately enough.
8
9
10
11
12

13 We further evaluate the exciton binding energy (E_b) that measures strength of the
14 Coulombic attraction in the photogenerated electron-hole pair. For 3-dimensional halide
15 perovskites, the excitons are mostly identified as the Wannier-Mott type where electron-hole
16 binding is weak and electron and hole densities are spatially delocalized.⁸⁰ From the effective
17 mass theory,⁹² the effective Bohr diameter of such an exciton can be estimated as,
18
19
20
21
22
23
24

$$a_0 = 2\hbar^2\epsilon^\infty/(e^2\mu) \quad (1)$$

25
26
27
28
29
30 where μ is the reduced carrier mass and ϵ^∞ is the effective dielectric constant at infinite
31 frequency. Empirical formula using the effective masses and dielectric constants further
32 define the binding energy of electron-hole pair in an exciton as follows,
33
34
35
36
37

$$E_b = 2\hbar^2/(\mu a_0^2) \quad (2)$$

38
39
40
41 Details of the Wannier-Mott type exciton in halide perovskites has been extensively
42 discussed by Manser *et al.*⁸⁰
43
44
45

46 Experimental Procedure

47 *Growth of MAPbBr_{3-x}Cl_x Single Crystals*

48
49
50
51 MAPbBr_{3-x}Cl_x single crystals were grown using the inverse temperature crystallization
52 technique. All materials used for single crystal growth were purchased and used as-received
53 including: N,N-Dimethylformamide (DMF) (Sigma Aldrich, anhydrous, 99.8%), PbBr₂ (Alfa
54
55
56
57
58
59
60

1
2
3 Aesar, Puratronic, 99.998%, metals basis), MABr (GreatCell Solar, >99%), MAcl (EMD
4 Millipore, >99.0%). Solutions were prepared using a 1:1 molar ratio of Pb precursor to
5 organic precursors. To obtain a specific percentage of Cl inclusion in solution, the organic
6 precursors (MABr and MAcl) were calculated and measured for 0%, 2%, 5%, 10%, 15%,
7 and 20 mol% Cl in the prepared single crystal growth solutions. Here, the organic precursor
8 was used for Cl inclusion in solution due to higher solubility in the $\text{MAPbBr}_{3-x}\text{Cl}_x$ solution.
9 Each solution was stirred for two hours at room temperature until completely dissolved. The
10 solutions were then filtered using 0.45 μm PTFE filters and separated into scintillation vials
11 with 2 mL each. The vials were then placed in an oil bath on a hot plate and heated to
12 $\approx 80^\circ\text{C}$ for final crystallization.

23 *Structural and Optical Characterization*

24
25 All experimental measurements were completed on single crystals, as grown. No post-
26 growth treatments were utilized. Single crystals were ground into fine powders, and Pow-
27 der XRD was used to characterize the lattice parameter of each Cl-dopant concentration.
28 The Powder XRD measurements were completed using a Rigaku Ultima III. JADE soft-
29 ware was used for Rietveld refinements for lattice parameters using the $\text{Pm}\bar{3}\text{m}$.cif file for
30 $\text{CH}_3\text{NH}_3\text{PbBr}_3$ received from the crystallography open database (COD ID 1545320). Opti-
31 cal measurements included UV-Vis absorption and photoluminescence. UV-Vis absorption
32 spectra were taken for each of the five different compositions of $\text{MAPbBr}_{3-x}\text{Cl}_x$ listed above
33 using transmission mode, then converted to Tauc plots to determine the band gap for each
34 single crystal composition. Three separate crystals from each composition were tested for
35 statistical analysis of the compositional band gaps. For photoluminescence measurements,
36 the same three crystals were tested for each composition. Three different spots on each of the
37 three crystals per composition were measured for statistical analysis of PL, to understand
38 the uniformity of the surfaces of each single crystalline composition. Radiation measure-
39 ments were performed in an aluminum light-sealed box to reduce the effect of noise from
40 light-interactions with the crystals. Here, we used a Keithley 6847 HV power supply, an
41
42
43
44
45
46
47
48
49
50
51
52
53
54
55
56
57
58
59
60

1
2
3 Ortec 142PC preamplifier with an Ortec 4002P preamp power supply, a low noise preampli-
4 fier filter SR560 (Stanford Research Systems), and a Tektronix PPO 4104 digital phosphor
5 oscilloscope. For spectra collection, we used an Ortec Dspec-Pro MCA paired with Maestro
6 v7.01 from Ortec.
7
8
9
10

11 12 13 Acknowledgement

14
15
16 The work at Los Alamos National Laboratory (LANL) was supported by the LANL Labo-
17 ratory Directed Research and Development Funds (LDRD) program. This work was done
18 in part at the Center for Nonlinear Studies (CNLS) and the Center for Integrated Nan-
19 otechnologies (CINT), a U.S. Department of Energy and Office of Basic Energy Sciences
20 user facility, at LANL. This research used resources provided by the LANL Institutional
21 Computing Program. Los Alamos National Laboratory is operated by Triad National Se-
22 curity, LLC, for the National Nuclear Security Administration of the U.S. Department of
23 Energy (Contract No. 89233218NCA000001). J.E. acknowledges the Institut Universitaire
24 de France.
25
26
27
28
29
30
31
32
33
34
35
36

37 Supporting Information Available

38
39
40 Electronic Supplementary Information (ESI) available: lattice parameter and structural
41 changes in $\text{MAPbBr}_{3-x}\text{Cl}_x$ with Cl incorporation, changes in electronic and optical prop-
42 erties, energy barriers of Br/Cl ion migration in the lattice, details of Helmholtz free energy.
43 This material is available free of charge via the Internet at <http://pubs.acs.org/>.
44
45
46
47
48
49

50 References

- 51
52
53 (1) Kojima, A.; Teshima, K.; Shirai, Y.; Miyasaka, T. Organometal Halide Perovskites as
54 Visible-light Sensitizers for Photovoltaic Cells. *J. Am. Chem. Soc.* **2009**, *131*, 6050–
55
56
57

- 6051.
- (2) Lee, M. M.; Teuscher, J.; Miyasaka, T.; Murakami, T. N.; Snaith, H. J. Efficient Hybrid Solar Cells Based on Meso-superstructured Organometal Halide Perovskites. *Science* **2012**, *338*, 643–647.
- (3) Green, M. A.; Ho-Baillie, A.; Snaith, H. J. The Emergence of Perovskite Solar Cells. *Nat. Photonics* **2014**, *8*, 506–514.
- (4) Grätzel, M. The Light and Shade of Perovskite Solar Cells. *Nat. Mater.* **2014**, *13*, 838–842.
- (5) Dou, L.; Yang, Y. M.; You, J.; Hong, Z.; Chang, W.-H.; Li, G.; Yang, Y. Solution-processed hybrid perovskite photodetectors with high detectivity. *Nat. Commun.* **2014**, *5*, 5404.
- (6) Snaith, H. J. Present status and future prospects of perovskite photovoltaics. *Nat. Mater.* **2018**, *17*, 372.
- (7) Jena, A. K.; Kulkarni, A.; Miyasaka, T. Halide perovskite photovoltaics: background, status, and future prospects. *Chem. Rev.* **2019**, *119*, 3036–3103.
- (8) Fang, Y.; Dong, Q.; Shao, Y.; Yuan, Y.; Huang, J. Highly narrowband perovskite single-crystal photodetectors enabled by surface-charge recombination. *Nat. Photonics* **2015**, *9*, 679.
- (9) Tan, Z.-K.; Moghaddam, R. S.; Lai, M. L.; Docampo, P.; Higler, R.; Deschler, F.; Price, M.; Sadhanala, A.; Pazos, L. M.; Credgington, D. Bright light-emitting diodes based on organometal halide perovskite. *Nat. Nanotechnol* **2014**, *9*, 687.
- (10) Yuan, M.; Quan, L. N.; Comin, R.; Walters, G.; Sabatini, R.; Voznyy, O.; Hoogland, S.; Zhao, Y.; Beauregard, E. M.; Kanjanaboos, P. Perovskite energy funnels for efficient light-emitting diodes. *Nat. Nanotechnol* **2016**, *11*, 872.

- 1
2
3 (11) Stranks, S. D.; Eperon, G. E.; Grancini, G.; Menelaou, C.; Alcocer, M. J.; Leijtens, T.;
4 Herz, L. M.; Petrozza, A.; Snaith, H. J. Electron-hole diffusion lengths exceeding 1
5 micrometer in an organometal trihalide perovskite absorber. *Science* **2013**, *342*, 341–
6 344.
7
8
9
10
11
12 (12) Protesescu, L.; Yakunin, S.; Bodnarchuk, M. I.; Krieg, F.; Caputo, R.; Hendon, C. H.;
13 Yang, R. X.; Walsh, A.; Kovalenko, M. V. Nanocrystals of cesium lead halide perovskites
14 (CsPbX₃, X= Cl, Br, and I): novel optoelectronic materials showing bright emission
15 with wide color gamut. *Nano Lett* **2015**, *15*, 3692–3696.
16
17
18
19
20
21 (13) Meggiolaro, D.; De Angelis, F. First-Principles Modeling of Defects in Lead Halide
22 Perovskites: Best Practices and Open Issues. *ACS Energy Lett* **2018**, *3*, 2206–2222.
23
24
25 (14) Pan, W.; Wu, H.; Luo, J.; Deng, Z.; Ge, C.; Chen, C.; Jiang, X.; Yin, W.-J.; Niu, G.;
26 Zhu, L. Cs₂AgBiBr₆ single-crystal X-ray detectors with a low detection limit. *Nat.*
27 *Photonics* **2017**, *11*, 726.
28
29
30
31
32 (15) He, Y.; Matei, L.; Jung, H. J.; McCall, K. M.; Chen, M.; Stoumpos, C. C.; Liu, Z.;
33 Peters, J. A.; Chung, D. Y.; Wessels, B. W. High spectral resolution of gamma-rays
34 at room temperature by perovskite CsPbBr₃ single crystals. *Nat. Commun.* **2018**, *9*,
35 1609.
36
37
38
39
40
41 (16) Wei, H.; Huang, J. Halide lead perovskites for ionizing radiation detection. *Nat. Com-*
42 *mun.* **2019**, *10*, 1066.
43
44
45 (17) Chen, Q.; Wu, J.; Ou, X.; Huang, B.; Almutlaq, J.; Zhumekenov, A. A.; Guan, X.;
46 Han, S.; Liang, L.; Yi, Z. All-inorganic perovskite nanocrystal scintillators. *Nature*
47 **2018**, *561*, 88.
48
49
50
51
52 (18) Wei, H.; DeSantis, D.; Wei, W.; Deng, Y.; Guo, D.; Savenije, T. J.; Cao, L.; Huang, J.
53 Dopant compensation in alloyed CH₃NH₃PbBr_{3-x}Cl_x perovskite single crystals
54 for gamma-ray spectroscopy. *Nat. Mater.* **2017**, *16*, 826.
55
56
57
58
59
60

- 1
2
3 (19) Saliba, M.; Matsui, T.; Seo, J.-Y.; Domanski, K.; Correa-Baena, J.-P.; Mohammad
4 K., N.; Zakeeruddin, S. M.; Tress, W.; Abate, A.; Hagfeldt, A.; Grätzel, M. Cesium-
5 containing Triple Cation Perovskite Solar Cells: Improved Stability, Reproducibility
6 and High Efficiency. *Energy Environ. Sci.* **2016**, *9*, 1989–1997.
7
8
9
10
11
12 (20) McMeekin, D. P.; Sadoughi, G.; Rehman, W.; Eperon, G. E.; Saliba, M.; Hörant-
13 ner, M. T.; Haghighirad, A.; Sakai, N.; Korte, L.; Rech, B.; Johnston, M. B.;
14 Herz, L. M.; Snaith, H. J. A Mixed-cation Lead Mixed-halide Perovskite Absorber
15 for Tandem Solar Cells. *Science* **2016**, *351*, 151–155.
16
17
18
19
20
21 (21) Ghosh, D.; Smith, A. R.; Walker, A. B.; Islam, M. S. Mixed A-Cation Perovskites for
22 Solar Cells: Atomic-Scale Insights Into Structural Distortion, Hydrogen Bonding, and
23 Electronic Properties. *Chem. Mater.* **2018**, *30*, 5194–5204.
24
25
26
27
28 (22) Jaffe, A.; Lin, Y.; Karunadasa, H. I. Halide Perovskites Under Pressure: Accessing New
29 Properties Through Lattice Compression. *ACS Energy Lett.* **2017**, *2*, 1549–1555.
30
31
32
33 (23) Kong, L.; Liu, G.; Gong, J.; Hu, Q.; Schaller, R. D.; Dera, P.; Zhang, D.; Liu, Z.;
34 Yang, W.; Zhu, K. Simultaneous band-gap narrowing and carrier-lifetime prolongation
35 of organic–inorganic trihalide perovskites. *Proc. Natl. Acad. Sci.* **2016**, *113*, 8910–8915.
36
37
38
39 (24) Zhang, X.; Li, L.; Sun, Z.; Luo, J. Rational chemical doping of metal halide perovskites.
40 *Chem. Soc. Rev.* **2019**, *48*, 517–539.
41
42
43
44 (25) Ghosh, D.; Walsh Atkins, P.; Islam, M. S.; Walker, A. B.; Eames, C. Good Vibrations:
45 Locking of Octahedral Tilting in Mixed-Cation Iodide Perovskites for Solar Cells. *ACS*
46 *Energy Lett.* **2017**, *2*, 2424–2429.
47
48
49
50
51 (26) Nagane, S.; Ghosh, D.; Hoye, R. L.; Zhao, B.; Ahmad, S.; Walker, A. B.; Islam, M. S.;
52 Ogale, S.; Sadhanala, A. Lead-Free Perovskite Semiconductors Based on Germanium–
53 Tin Solid Solutions: Structural and Optoelectronic Properties. *J. Phys. Chem. C* **2018**,
54 *122*, 5940–5947.
55
56
57
58
59
60

- 1
2
3 (27) Ghosh, D.; Aziz, A.; Dawson, J. A.; Walker, A. B.; Islam, M. S. Putting the Squeeze
4 on Lead Iodide Perovskites: Pressure-Induced Effects to Tune their Structural and
5 Optoelectronic Behaviour. *Chem. Mater* **2019**, *31*, 4063.
6
7
8
9
10 (28) Xing, G.; Mathews, N.; Sun, S.; Lim, S. S.; Lam, Y. M.; Grätzel, M.; Mhaisalkar, S.;
11 Sum, T. C. Long-range balanced electron-and hole-transport lengths in organic-
12 inorganic $\text{CH}_3\text{NH}_3\text{PbI}_3$. *Science* **2013**, *342*, 344–347.
13
14
15
16 (29) Chen, Q.; Zhou, H.; Fang, Y.; Stieg, A. Z.; Song, T.-B.; Wang, H.-H.; Xu, X.; Liu, Y.;
17 Lu, S.; You, J. The optoelectronic role of chlorine in $\text{CH}_3\text{NH}_3\text{PbI}_3$ (Cl)-based
18 perovskite solar cells. *Nat. Commun.* **2015**, *6*, 7269.
19
20
21
22 (30) Yantara, N.; Yanan, F.; Shi, C.; Dewi, H. A.; Boix, P. P.; Mhaisalkar, S. G.; Mathews, N.
23 Unravelling the effects of Cl addition in single step $\text{CH}_3\text{NH}_3\text{PbI}_3$ perovskite solar cells.
24
25
26
27
28
29
30 (31) Nie, W.; Tsai, H.; Asadpour, R.; Blancon, J.-C.; Neukirch, A. J.; Gupta, G.; Cro-
31 chet, J. J.; Chhowalla, M.; Tretiak, S.; Alam, M. A. High-efficiency solution-processed
32 perovskite solar cells with millimeter-scale grains. *Science* **2015**, *347*, 522–525.
33
34
35
36 (32) Yang, B.; Keum, J.; Ovchinnikova, O. S.; Belianinov, A.; Chen, S.; Du, M.-H.;
37 Ivanov, I. N.; Rouleau, C. M.; Geohegan, D. B.; Xiao, K. Deciphering halogen com-
38 petition in organometallic halide perovskite growth. *J. Am. Chem. Soc.* **2016**, *138*,
39 5028–5035.
40
41
42
43
44 (33) Dar, M. I.; Arora, N.; Gao, P.; Ahmad, S.; Gratzel, M.; Nazeeruddin, M. K. Investi-
45 gation regarding the role of chloride in organic–inorganic halide perovskites obtained
46 from chloride containing precursors. *Nano Lett* **2014**, *14*, 6991–6996.
47
48
49
50
51 (34) Tidhar, Y.; Edri, E.; Weissman, H.; Zohar, D.; Hodes, G.; Cahen, D.; Rybtchinski, B.;
52 Kirmayer, S. Crystallization of methyl ammonium lead halide perovskites: implications
53 for photovoltaic applications. *J. Am. Chem. Soc.* **2014**, *136*, 13249–13256.
54
55
56
57
58
59
60

- 1
2
3 (35) Zhang, M.; Yu, H.; Lyu, M.; Wang, Q.; Yun, J.-H.; Wang, L. Composition-dependent
4 photoluminescence intensity and prolonged recombination lifetime of perovskite CH₃
5 NH₃PbBr_{3-x}Cl_x films. *Chem Commun* **2014**, *50*, 11727–11730.
6
7
8
9
10 (36) Wei, M.; Chung, Y.-H.; Xiao, Y.; Chen, Z. Color tunable halide perovskite
11 CH₃NH₃PbBr_{3-x}Cl_x emission via annealing. *Org Electron*. **2015**, *26*, 260–264.
12
13
14
15 (37) Edri, E.; Kirmayer, S.; Kulbak, M.; Hodes, G.; Cahen, D. Chloride inclusion and hole
16 transport material doping to improve methyl ammonium lead bromide perovskite-based
17 high open-circuit voltage solar cells. *J. Phys. Chem. Lett* **2014**, *5*, 429–433.
18
19
20
21 (38) Zhang, F.; Zhong, H.; Chen, C.; Wu, X.-g.; Hu, X.; Huang, H.; Han, J.; Zou, B.;
22 Dong, Y. Brightly luminescent and color-tunable colloidal CH₃NH₃PbX₃ (X= Br, I,
23 Cl) quantum dots: potential alternatives for display technology. *ACS Nano* **2015**, *9*,
24 4533–4542.
25
26
27
28
29
30 (39) Kim, Y.-H.; Cho, H.; Heo, J. H.; Kim, T.-S.; Myoung, N.; Lee, C.-L.; Im, S. H.; Lee, T.-
31 W. Multicolored organic/inorganic hybrid perovskite light-emitting diodes. *Adv. Mater.*
32 **2015**, *27*, 1248–1254.
33
34
35
36
37 (40) Tisdale, J. T.; Smith, T.; Salasin, J. R.; Ahmadi, M.; Johnson, N.; Ievlev, A. V.;
38 Koehler, M.; Rawn, C. J.; Lukosi, E.; Hu, B. Precursor purity effects on solution-based
39 growth of MAPbBr₃ single crystals towards efficient radiation sensing. *CrystEngComm*
40 **2018**, *20*, 7818–7825.
41
42
43
44
45
46 (41) Xu, Q.; Wei, H.; Wei, W.; Chuirazzi, W.; DeSantis, D.; Huang, J.; Cao, L. Detec-
47 tion of charged particles with a methylammonium lead tribromide perovskite single
48 crystal. *Nuclear Instruments and Methods in Physics Research Section A: Accelerators,*
49 *Spectrometers, Detectors and Associated Equipment* **2017**, *848*, 106–108.
50
51
52
53
54
55 (42) He, Y.; Ke, W.; Alexander, G. C.; McCall, K. M.; Chica, D. G.; Liu, Z.; Hadar, I.;
56
57
58
59
60

- 1
2
3 Stoumpos, C. C.; Wessels, B. W.; Kanatzidis, M. G. Resolving the Energy of γ -Ray
4 Photons with MAPbI₃ Single Crystals. *ACS Photonics* **2018**, *5*, 4132–4138.
5
6
7
8 (43) Lukosi, E.; Smith, T.; Tisdale, J.; Hamm, D.; Seal, C.; Hu, B.; Ahmadi, M. Methylam-
9 monium lead tribromide semiconductors: Ionizing radiation detection and electronic
10 properties. *Nuclear Instruments and Methods in Physics Research Section A: Acceler-*
11 *ators, Spectrometers, Detectors and Associated Equipment* **2019**, *927*, 401–406.
12
13
14
15
16
17 (44) Kim, S.-Y.; Lee, H.-C.; Nam, Y.; Yun, Y.; Lee, S.-H.; Kim, D. H.; Noh, J. H.; Lee, J.-
18 H.; Kim, D.-H.; Lee, S. Ternary diagrams of the phase, optical bandgap energy and
19 photoluminescence of mixed-halide perovskites. *Acta Mater.* **2019**, *181*, 460–469.
20
21
22
23
24 (45) Rosales, B. A.; Men, L.; Cady, S. D.; Hanrahan, M. P.; Rossini, A. J.; Vela, J. Persistent
25 dopants and phase segregation in organolead mixed-halide perovskites. *Chem. Mater.*
26 **2016**, *28*, 6848–6859.
27
28
29
30
31 (46) Bischak, C. G.; Hetherington, C. L.; Wu, H.; Aloni, S.; Ogletree, D. F.; Limmer, D. T.;
32 Ginsberg, N. S. Origin of reversible photoinduced phase separation in hybrid per-
33 ovskites. *Nano Lett* **2017**, *17*, 1028–1033.
34
35
36
37
38 (47) Pan, D.; Fu, Y.; Chen, J.; Czech, K. J.; Wright, J. C.; Jin, S. Visualization and studies
39 of ion-diffusion kinetics in cesium lead bromide perovskite nanowires. *Nano Lett.* **2018**,
40 *18*, 1807–1813.
41
42
43
44 (48) Jang, D. M.; Park, K.; Kim, D. H.; Park, J.; Shojaei, F.; Kang, H. S.; Ahn, J.-P.;
45 Lee, J. W.; Song, J. K. Reversible halide exchange reaction of organometal trihalide
46 perovskite colloidal nanocrystals for full-range band gap tuning. *Nano Lett.* **2015**, *15*,
47 5191–5199.
48
49
50
51
52
53 (49) Yin, W.-J.; Yan, Y.; Wei, S.-H. Anomalous alloy properties in mixed halide perovskites.
54 *J. Phys. Chem. Lett* **2014**, *5*, 3625–3631.
55
56
57
58
59
60

- 1
2
3 (50) Brivio, F.; Caetano, C.; Walsh, A. Thermodynamic origin of photoinstability in the
4 CH₃NH₃Pb (I_{1-x} Br_x)₃ hybrid halide perovskite alloy. *J. Phys. Chem. Lett.* **2016**,
5 7, 1083–1087.
6
7
8
9
10 (51) Chen, T.; Foley, B. J.; Park, C.; Brown, C. M.; Harriger, L. W.; Lee, J.; Ruff, J.;
11 Yoon, M.; Choi, J. J.; Lee, S.-H. Entropy-driven Structural Transition and Kinetic
12 Trapping in Formamidinium Lead Iodide Perovskite. *Sci. Adv.* **2016**, 2, e1601650.
13
14
15
16 (52) Noh, J. H.; Im, S. H.; Heo, J. H.; Mandal, T. N.; Seok, S. I. Chemical management for
17 colorful, efficient, and stable inorganic–organic hybrid nanostructured solar cells. *Nano*
18 *Lett.* **2013**, 13, 1764–1769.
19
20
21
22
23 (53) Comin, R.; Walters, G.; Thibau, E. S.; Voznyy, O.; Lu, Z.-H.; Sargent, E. H. Structural,
24 optical, and electronic studies of wide-bandgap lead halide perovskites. *J. Mater. Chem.*
25 *C* **2015**, 3, 8839–8843.
26
27
28
29
30 (54) Sadhanala, A.; Ahmad, S.; Zhao, B.; Giesbrecht, N.; Pearce, P. M.; Deschler, F.;
31 Hoye, R. L.; Godel, K. C.; Bein, T.; Docampo, P. Blue-green color tunable solution
32 processable organolead chloride–bromide mixed halide perovskites for optoelectronic
33 applications. *Nano Lett.* **2015**, 15, 6095–6101.
34
35
36
37
38
39 (55) Zhang, T.; Yang, M.; Benson, E. E.; Li, Z.; van de Lagemaat, J.; Luther, J. M.; Yan, Y.;
40 Zhu, K.; Zhao, Y. A facile solvothermal growth of single crystal mixed halide perovskite
41 CH₃NH₃Pb (Br_{1-x} Cl_x)₃. *Chem. Commun.* **2015**, 51, 7820–7823.
42
43
44
45
46 (56) Menéndez-Proupin, E.; Palacios, P.; Wahnón, P.; Conesa, J. Self-consistent relativistic
47 band structure of the CH₃NH₃PbI₃ perovskite. *Phys Rev B* **2014**, 90, 045207.
48
49
50
51 (57) Even, J.; Pedesseau, L.; Jancu, J.-M.; Katan, C. Importance of spin–orbit coupling in
52 hybrid organic/inorganic perovskites for photovoltaic applications. *J. Phys. Chem. Lett*
53 **2013**, 4, 2999–3005.
54
55
56
57
58
59
60

- 1
2
3 (58) Bandiello, E.; Ávila, J.; Gil-Escrig, L.; Tekelenburg, E.; Sessolo, M.; Bolink, H. J. In-
4 fluence of Mobile Ions on the Electroluminescence Characteristics of Methylammonium
5 Lead Iodide Perovskite Diodes. *J. Mater. Chem. A* **2016**, *4*, 18614–18620.
6
7
8
9
10 (59) Frost, J. M.; Walsh, A. What Is Moving in Hybrid Halide Perovskite Solar Cells? *Acc.*
11 *Chem. Res.* **2016**, *49*, 528–535.
12
13
14 (60) Yuan, Y.; Huang, J. Ion migration in organometal trihalide perovskite and its impact
15 on photovoltaic efficiency and stability. *Acc. Chem. Res* **2016**, *49*, 286–293.
16
17
18
19 (61) Snaith, H. J.; Abate, A.; Ball, J. M.; Eperon, G. E.; Leijtens, T.; Noel, N. K.;
20 Stranks, S. D.; Wang, J. T.-W.; Wojciechowski, a.; et., Anomalous Hysteresis in Per-
21 ovskite Solar Cells. *J. Phys. Chem. Lett.* **2014**, *5*, 1511–1515.
22
23
24
25 (62) Xiao, Z.; Yuan, Y.; Shao, Y.; Wang, Q.; Dong, Q.; Bi, C.; Sharma, P.; Gruverman, A.;
26 Huang, J. Giant switchable photovoltaic effect in organometal trihalide perovskite de-
27 vices. *Nat. Mater.* **2015**, *14*, 193–198.
28
29
30
31
32 (63) Tress, W.; Marinova, N.; Moehl, T.; Zakeeruddin, S. M.; Nazeeruddin, M. K.;
33 Grätzel, M. Understanding the rate-dependent J–V hysteresis, slow time component,
34 and aging in CH₃NH₃PbI₃ perovskite solar cells: the role of a compensated electric
35 field. *Energ. Environ. Sci* **2015**, *8*, 995–1004.
36
37
38
39
40 (64) Lin, Q.; Armin, A.; Nagiri, R. C. R.; Burn, P. L.; Meredith, P. Electro-optics of per-
41 ovskite solar cells. *Nat. Photonics* **2015**, *9*, 106–112.
42
43
44 (65) Ferdani, D.; Pering, S.; Ghosh, D.; Kubiak, P.; Walker, A.; Lewis, S. E.; Johnson, A. L.;
45 Baker, P. J.; Islam, S.; Cameron, P. J. Partial Cation Substitution Reduces Iodide Ion
46 Transport in Lead Iodide Perovskite Solar Cells. *Energ. Environ. Sci* **2019**,
47
48
49
50
51
52 (66) Henkelman, G.; Uberuaga, B. P.; Jonsson, H. Climbing image nudged elastic band
53
54
55
56
57
58
59
60

- 1
2
3 method for finding saddle points and minimum energy paths. *J. Chem. Phys* **2000**,
4 *113*, 9901–9904.
5
6
7
8 (67) Eames, C.; Frost, J. M.; Barnes, P. R.; O’regan, B. C.; Walsh, A.; Islam, M. S. Ionic
9 Transport in Hybrid Lead Iodide Perovskite Solar Cells. *Nat. Commun.* **2015**, *6*, 7497.
10
11
12 (68) Meloni, S.; Moehl, T.; Tress, W.; Franckevičius, M.; Saliba, M.; Lee, Y. H.; Gao, P.;
13 Nazeeruddin, M. K.; Zakeeruddin, S. M.; Rothlisberger, U. Ionic polarization-induced
14 current–voltage hysteresis in CH₃NH₃PbX₃ perovskite solar cells. *Nat. Commun.*
15 **2016**, *7*, 10334.
16
17
18
19
20
21 (69) Kennard, R. M.; Dahlman, C. J.; Nakayama, H.; DeCrescent, R. A.; Schuller, J. A.;
22 Seshadri, R.; Mukherjee, K.; Chabynyc, M. L. Phase stability and diffusion in lat-
23 eral heterostructures of methyl ammonium lead halide perovskites. *ACS Appl. Energy*
24 *Mater.* **2019**, *11*, 25313–25321.
25
26
27
28
29
30 (70) García-Rodríguez, R.; Ferdani, D.; Pering, S.; Baker, P. J.; Cameron, P. J. Influence of
31 bromide content on iodide migration in inverted MAPb (I_{1-x}Br_x)₃ perovskite solar
32 cells. *J. Mater. Chem. A* **2019**, *7*, 22604–22614.
33
34
35
36
37 (71) Lin, C.; Li, S.; Zhang, W.; Shao, C.; Yang, Z. Effect of Bromine Substitution on the
38 Ion Migration and Optical Absorption in MAPbI₃ Perovskite Solar Cells: The First-
39 Principles Study. *ACS Appl. Energy Mater.* **2018**, *1*, 1374–1380.
40
41
42
43 (72) Tisdale, J. T.; Muckley, E.; Ahmadi, M.; Smith, T.; Seal, C.; Lukosi, E.; Ivanov, I. N.;
44 Hu, B. Dynamic Impact of Electrode Materials on Interface of Single-Crystalline Methy-
45 lammonium Lead Bromide Perovskite. *Adv. Mater. Interfaces* **2018**, *5*, 1800476.
46
47
48
49
50 (73) Galkowski, K.; Mitioglu, A.; Miyata, A.; Plochocka, P.; Portugall, O.; Eperon, G. E.;
51 Wang, J. T.-W.; Stergiopoulos, T.; Stranks, S. D.; Snaith, H. J. Determination of the
52 exciton binding energy and effective masses for methylammonium and formamidinium
53 lead tri-halide perovskite semiconductors. *Energ. Environ. Sci* **2016**, *9*, 962–970.
54
55
56
57
58
59
60

- 1
2
3 (74) Mosconi, E.; Umari, P.; De Angelis, F. Electronic and optical properties of MAPbX₃
4 perovskites (X= I, Br, Cl): a unified DFT and GW theoretical analysis. *Phys. Chem.*
5 *Chem. Phys* **2016**, *18*, 27158–27164.
6
7
8
9
10 (75) Miyata, A.; Mitioglu, A.; Plochocka, P.; Portugall, O.; Wang, J. T.-W.; Stranks, S. D.;
11 Snaith, H. J.; Nicholas, R. J. Direct measurement of the exciton binding energy and
12 effective masses for charge carriers in organic–inorganic tri-halide perovskites. *Nature*
13 *Physics* **2015**, *11*, 582.
14
15
16
17
18 (76) D’Innocenzo, V.; Grancini, G.; Alcocer, M. J.; Kandada, A. R. S.; Stranks, S. D.;
19 Lee, M. M.; Lanzani, G.; Snaith, H. J.; Petrozza, A. Excitons versus free charges in
20 organo-lead tri-halide perovskites. *Nat. Commun.* **2014**, *5*, 3586.
21
22
23
24
25 (77) Herz, L. M. Charge-carrier mobilities in metal halide perovskites: Fundamental mech-
26 anisms and limits. *ACS Energy Lett.* **2017**, *2*, 1539–1548.
27
28
29
30 (78) Yamada, T.; Aharen, T.; Kanemitsu, Y. Near-band-edge optical responses of CH₃NH
31 ₃PbCl₃ single crystals: photon recycling of excitonic luminescence. *Phys. Rev. Lett.*
32 **2018**, *120*, 057404.
33
34
35
36 (79) Saba, M.; Quochi, F.; Mura, A.; Bongiovanni, G. Excited state properties of hybrid
37 perovskites. *Acc. Chem. Res* **2015**, *49*, 166–173.
38
39
40
41 (80) Manser, J. S.; Christians, J. A.; Kamat, P. V. Intriguing optoelectronic properties of
42 metal halide perovskites. *Chem. Rev.* **2016**, *116*, 12956–13008.
43
44
45
46 (81) Sestu, N.; Cadelano, M.; Sarritzu, V.; Chen, F.; Marongiu, D.; Piras, R.; Mainas, M.;
47 Quochi, F.; Saba, M.; Mura, A. Absorption F-sum rule for the exciton binding energy
48 in methylammonium lead halide perovskites. *J. Phys. Chem. Lett* **2015**, *6*, 4566–4572.
49
50
51
52 (82) Tanaka, K.; Takahashi, T.; Ban, T.; Kondo, T.; Uchida, K.; Miura, N. Compara-
53
54
55
56
57
58
59
60

- tive study on the excitons in lead-halide-based perovskite-type crystals $\text{CH}_3\text{NH}_3\text{PbBr}_3$ $\text{CH}_3\text{NH}_3\text{PbI}_3$. *Solid State Commun.* **2003**, *127*, 619–623.
- (83) Yakunin, S.; Dirin, D. N.; Shynkarenko, Y.; Morad, V.; Cherniukh, I.; Nazarenko, O.; Kreil, D.; Nauser, T.; Kovalenko, M. V. Detection of gamma photons using solution-grown single crystals of hybrid lead halide perovskites. *Nat. Photonics* **2016**, *10*, 585.
- (84) Nazarenko, O.; Yakunin, S.; Morad, V.; Cherniukh, I.; Kovalenko, M. V. Single crystals of caesium formamidinium lead halide perovskites: solution growth and gamma dosimetry. *NPG Asia Materials* **2017**, *9*, e373.
- (85) Kresse, G.; Hafner, J. Ab initio molecular dynamics for liquid metals. *Phys. Rev. B* **1993**, *47*, 558.
- (86) Kresse, G.; Hafner, J. Ab initio molecular-dynamics simulation of the liquid-metal–amorphous-semiconductor transition in germanium. *Phys. Rev. B* **1994**, *49*, 14251.
- (87) Kresse, G.; Joubert, D. From ultrasoft pseudopotentials to the projector augmented-wave method. *Phys. Rev. B* **1999**, *59*, 1758.
- (88) Perdew, J. P.; Burke, K.; Ernzerhof, M. Generalized Gradient Approximation Made Simple. *Phys. Rev. Lett.* **1996**, *77*, 3865.
- (89) Grimme, S.; Antony, J.; Ehrlich, S.; Krieg, H. A consistent and accurate ab initio parametrization of density functional dispersion correction (DFT-D) for the 94 elements H–Pu. *J. Chem. Phys.* **2010**, *132*, 154104.
- (90) Leguy, A. M.; Goñi, A. R.; Frost, J. M.; Skelton, J.; Brivio, F.; Rodríguez-Martínez, X.; Weber, O. J.; Pallipurath, A.; Alonso, M. I.; Campoy-Quiles, M. Dynamic disorder, phonon lifetimes, and the assignment of modes to the vibrational spectra of methylammonium lead halide perovskites. *Phys. Chem. Chem. Phys.* **2016**, *18*, 27051–27066.

- 1
2
3 (91) Ganose, A. M.; Jackson, A. J.; Scanlon, D. O. sumo: Command-line tools for plotting
4 and analysis of periodic ab initio calculations. *J. Open Source Softw.* **2018**, *2*.
5
6
7
8 (92) Stoneham, A. M. *Theory of defects in solids: electronic structure of defects in insulators*
9 *and semiconductors*; Oxford University Press: Oxford, UK, 2001.
10
11

